

# NONCONVEX RECONSTRUCTION FOR LOW-DIMENSIONAL FLUORESCENCE MOLECULAR TOMOGRAPHIC POISSON OBSERVATIONS

*Lasith Adhikari<sup>1</sup>, Dianwen Zhu<sup>2</sup>, Changqing Li<sup>2</sup> and Roummel F. Marcia<sup>1</sup>*

<sup>1</sup>Department of Applied Mathematics, University of California, Merced, Merced, CA 95343 USA

<sup>2</sup>School of Engineering, University of California Merced, Merced, CA 95343 USA

## ABSTRACT

As an emerging near-infrared molecular imaging modality, fluorescence molecular tomography (FMT) has great potential in resolving the molecular and cellular processes in 3D objects through the reconstruction of the injected fluorescence probe concentration. In practice, when a charge-coupled device (CCD) camera is used to obtain FMT measurements, the observations are corrupted by noise which follows a Poisson distribution. To reconstruct the original concentration, the standard least-squares function for data-fitting is not a suitable objective function to minimize since this model assumes measurement noise which follows a Gaussian distribution. Rather, in this paper, we minimize a negative log-likelihood function to more accurately model the CCD camera shot noise. Furthermore, we exploit the presence of the fluorescence in only small regions of the 3D object by introducing a non-convex penalty term that promotes sparsity in the reconstruction. This paper proposes a method to solve the FMT reconstruction problem from low-dimensional and low-mean photon count measurements. Using simulated data, we validate the effectiveness of the proposed non-convex Poisson-based reconstruction method for FMT inverse problems.

**Index Terms**— Fluorescence molecular tomography, non-convex optimization, Poisson observations, sparse reconstruction,  $\ell_p$ -norm

## 1. INTRODUCTION

Fluorescence molecular tomography (FMT) is a promising noninvasive functional imaging technique due to the high availability of fluorescent dyes, high sensitivity of imaging and low instrumental cost [1]. FMT has been widely used for comprehensive investigation of molecular level activities in cancer detection, development of new drugs, visualization of gene expression and assessment of therapy [2, 3]. In FMT, near-infrared laser beams excite the injected fluorescence probe such as fluorophores within the object and then the emitted fluorescent signals from the probe are captured by a charge-coupled device (CCD) camera. In practice, those

measurements are contaminated by noise which follows a Poisson distribution [4]. When a sufficiently large number of photons are collected at the detector end, the noise can be modeled well by a Gaussian distribution. In this case, the internal fluorescence probe concentration is usually recovered by minimizing the discrepancy between the boundary measurements and the forward predictions using a least-squares data-fitting term [5].

Since only the photon distribution over the tissue boundary is measured by the CCD camera, FMT reconstruction problem is often ill-posed. This is usually alleviated by obtaining a large number of measurement data. In addition, the system matrix is ill-conditioned due to the high scattering and high absorption of the photons which leads to a very unstable system [6]. In order to obtain a unique solution, the FMT problem is often regularized using a Tikhonov (e.g., the  $\ell_2$ -norm) regularization term. The  $\ell_2$ -norm regularized problem is simple and efficient to solve using gradient based methods; however, the resulting solution is typically over-smoothed with non-localized targets [7]. Since the target that we would like to reconstruct is relatively small compared to the entire reconstruction domain, the resulting reconstructed signal should be sparse. With this prior knowledge, a sparse solution can be achieved by incorporating the  $\ell_0$ -norm constraint, which counts the number of non-zero entries in the solution, to the original problem. Solving the  $\ell_0$ -norm minimization problem is NP-hard and computationally infeasible for high-dimensional problems [8]. As a good approximation to the  $\ell_0$ -norm, the convex  $\ell_1$ -norm regularization has been used to promote the sparsity of the solution [9]. However, the nonconvex  $\ell_p$ -norm ( $0 \leq p < 1$ ) regularization has been shown to provide a sparser solution in FMT imaging [10]. Very recently, a nonuniform weighting method in combination with  $\ell_1$  regularization for FMT was proposed in [11], which was shown to outperform the method in [10] that was based on a uniform weighting scheme.

Almost all of the aforementioned results assumed Gaussian-type noises and are based on the least-square model. In the rare cases where the Poisson noise was considered in solving the FMT problem, such as in a recent work of Yu [12], the least-squares model was still used as objective function. In this paper, based on [13, 14], we propose to solve the

This work was supported by National Science Foundation Grant CMMI-1333326.

ill-posed, ill-conditioned FMT reconstruction problem only using a relatively small number of observations with Poisson noise. Using simulated FMT data with different Poisson noise levels, we compare the performance of the proposed method with the newest Gaussian-based Non-Uniform Multiplicative weighting with Ordered Subsets (NUMOS) algorithm [11] with respect to different image quality metrics.

## 2. RECONSTRUCTION METHODOLOGY

In an FMT imaging system, the propagation of both excitation photons and fluorescence emission photons in scattering media such as tissues is usually approximated by the diffusion equation, which can be solved by the finite element method (FEM), leading to a simple linear system of equations [5, 15]:  $\mathbf{A}\mathbf{f} = \mathbf{y}$ . Since the arrival of photons at the detector end has low photon count which follows a Poisson process model [16], the measurement can be better modeled as follows

$$\mathbf{y} \sim \text{Poisson}(\mathbf{A}\mathbf{f}^*),$$

where  $\mathbf{y} \in \mathbb{Z}_+^m$  is a vector of measured photon counts,  $\mathbf{f}^* \in \mathbb{R}_+^n$  is the true signal of interest, and  $\mathbf{A} \in \mathbb{R}_+^{m \times n}$  is the system matrix. The unknown Poisson parameter  $\mathbf{A}\mathbf{f}^*$  is determined by the *maximum likelihood principle*. In this section, we briefly describe the Poisson-based and Gaussian-based algorithms that we use to reconstruct the signal  $\mathbf{f}^*$  from low-dimensional FMT observations  $\mathbf{y}$ .

### 2.1. Poisson-based reconstruction methods

In general, the Poisson intensity reconstruction problem has the form:

$$\begin{aligned} & \underset{\mathbf{f} \in \mathbb{R}^n}{\text{minimize}} && \Phi(\mathbf{f}) \equiv F(\mathbf{f}) + \tau \text{pen}(\mathbf{f}) \\ & \text{subject to} && \mathbf{f} \succeq 0, \end{aligned} \quad (1)$$

where  $\tau > 0$ ,  $F(\mathbf{f})$  is the negative Poisson log-likelihood function

$$F(\mathbf{f}) = \mathbf{1}^T \mathbf{A}\mathbf{f} - \sum_{i=1}^m y_i \log(e_i^T \mathbf{A}\mathbf{f} + \beta),$$

where  $\mathbf{1}$  is an  $m$ -vector of ones,  $\mathbf{e}_i$  is the  $i$ th canonical basis unit vector,  $\beta > 0$  (typically  $\beta \ll 1$ ) and  $\text{pen} : \mathbb{R}^n \rightarrow \mathbb{R}$  is a penalty function [17]. In [13], the optimal solution of (1) is obtained by minimizing a sequence of quadratic surrogate functions for  $F(\mathbf{f})$ , where the Hessian is replaced by a scaled identity matrix. This approximation can be simplified to a subproblem of the form

$$\begin{aligned} \mathbf{f}^{k+1} &= \underset{\mathbf{f} \in \mathbb{R}^n}{\text{arg min}} && \frac{1}{2} \|\mathbf{f} - \mathbf{s}^k\|_2^2 + \frac{\tau}{\alpha_k} \text{pen}(\mathbf{f}) \\ & \text{subject to} && \mathbf{f} \succeq 0, \end{aligned} \quad (2)$$

where

$$\mathbf{s}^k = \mathbf{f}^k - \frac{1}{\alpha_k} \nabla F(\mathbf{f}^k) \quad \text{and} \quad \alpha_k > 0.$$

By replacing the penalty term  $\text{pen}(\mathbf{f})$  in (2) by  $\|\mathbf{f}\|_1$  and  $\|\mathbf{f}\|_p^p$ , we can obtain the Sparse Poisson Intensity Reconstruction ALgorithm (SPIRAL): SPIRAL- $\ell_1$  [13] and SPIRAL- $\ell_p$  [14] constrained optimization subproblems, respectively.

If  $\text{pen}(\mathbf{f}) = \|\mathbf{f}\|_1$  in (2), then the optimal solution to the SPIRAL- $\ell_1$  minimization subproblem (2) has the following closed form solution:

$$\mathbf{f}^{k+1} = \left( \mathbf{s}^k - \frac{\tau}{\alpha_k} \mathbf{1} \right)_+,$$

where the operation  $(\cdot)_+ = \max\{0, \cdot\}$  is component-wise.

If  $\text{pen}(\mathbf{f}) = \|\mathbf{f}\|_p^p$  in (2), then the SPIRAL- $\ell_p$  minimization subproblem (2) can be uncoupled into scalar minimization problems of the form

$$f^* = \underset{f \in \mathbb{R}}{\text{arg min}} \quad \Omega(f) = \frac{1}{2}(f - s)^2 + \lambda|f|^p, \quad (3)$$

where  $f$  and  $s$  are general elements of the vectors  $\mathbf{f}$  and  $\mathbf{s}^k$  respectively and  $\lambda = \tau/\alpha_k$ . The optimal solution of the scalar minimization problem (3) is given by the generalized soft-thresholding [18] function

$$f^* = \begin{cases} 0, & \text{if } |s| \leq \gamma_p(\lambda) \\ \text{sgn}(s)S_p(|s|, \lambda), & \text{if } |s| > \gamma_p(\lambda), \end{cases}$$

where the threshold value  $\gamma_p(\lambda)$  is computed by

$$\gamma_p(\lambda) = (2\lambda(1-p))^{\frac{1}{2-p}} + \lambda p(2\lambda(1-p))^{\frac{p-1}{2-p}},$$

and  $S_p(|s|, \lambda)$  is the appropriate root of the equation

$$\Omega'(S_p(|s|, \lambda)) = S_p(|s|, \lambda) - s + \lambda p(S_p(|s|, \lambda))^{p-1} = 0.$$

(See [14] for details.)

### 2.2. Gaussian-based reconstruction methods

In [11], the NUMOS algorithm reconstructs an unknown signal  $\mathbf{f}^*$  by solving the  $\ell_2 - \ell_1$  constraint minimization problem:

$$\mathbf{f}^* = \underset{\mathbf{f} \succeq 0}{\text{arg min}} \quad \frac{1}{2} \|\mathbf{A}\mathbf{f} - \mathbf{y}\|_2^2 + \tau \|\mathbf{f}\|_1. \quad (4)$$

Similar to problem (2), the optimal solution to the problem (4) is also obtained from an iterative updating of a series of quadratic surrogate functions. The difference is that the surrogate functions for NUMOS algorithm are constructed using a nonuniform type of weighting scheme [11]. The next iterate  $\mathbf{f}^{k+1}$  is given by the following analytic formula, where the vector multiplication and division are component-wise:

$$\mathbf{f}^{k+1} = \mathbf{f}^k \frac{(\mathbf{A}^T \mathbf{y} - \tau \mathbf{1})_+}{\mathbf{A}^T \mathbf{A} \mathbf{f}^k}.$$

### 2.3. Image Quality Metrics

In order to compare the image qualities of the reconstructions obtained by the methods explained previously, we use the same metrics used in [10, 11], which are listed below:

$$\begin{aligned} \text{VR} &= \frac{|\text{rROI}|}{|\text{ROI}|}, \\ \text{Dice} &= \frac{2 * |\text{rROI} \cap \text{ROI}|}{|\text{rROI}| + |\text{ROI}|}, \\ \text{CNR} &= \frac{\text{Mean}(f_{\text{ROI}}) - \text{Mean}(f_{\text{ROB}})}{\sqrt{\omega_{\text{ROI}} \text{Var}(f_{\text{ROI}}) + (1 - \omega_{\text{ROI}}) \text{Var}(f_{\text{ROB}})}}, \\ \text{MSE} &= \frac{1}{N} \sum_{j=1}^N (f_j - f_j^*)^2. \end{aligned}$$

The Volume Ratio (VR) [19] measures the ratio between the true region of interest (ROI) and the reconstructed region of interest (rROI), where  $|\cdot|$  denotes the number of elements of the set, and the rROI contains the reconstructed signals with amplitudes higher than half of the maximum amplitude of all reconstructed signals. Ideally, VR should be close to 1. The dice similarity coefficient (Dice) [20] measures the location accuracy of the reconstructed target with respect to the true location. In the ideal case, Dice should also be close to 1. The Contrast-to-Noise Ratio (CNR) [21] measures how easy it is to see the reconstructed target from the background, where  $\omega_{\text{ROI}} = |\text{ROI}| / (|\text{ROI}| + |\text{ROB}|)$ , ROB is the true background region and  $f$  denotes the reconstructed signal. A high CNR value means a high contrast between the reconstructed target and the background, which is preferred. The Mean Square Error (MSE) measures the difference between the approximation and the truth, where  $f^*$  is the true signal.

### 3. NUMERICAL EXPERIMENTS

In this study, we simulated a 3D cubic phantom with two embedded fluorescence capillary rod targets as shown in Fig.2. For the FEM mesh, there are a total of 8,690 nodes inside the 3D cube while only 36 nodes are located inside the two rods. The fluorophore concentration of the nodes is set to 7,000 inside the two rods and 0 outside. We chose a total of 20 excitation source positions and 1,057 detector positions on the top surface of the cube, which gives us  $20 \times 1,057 = 21,140$  measurements. But we used only around 1/10 th of all the measurements (i.e. 2,120 measurements). We assumed that the excitation wavelength is 650 nm and the emission wavelength is 720 nm. The tissue optical properties were  $\mu_a = 0.0022 \text{ mm}^{-1}$ ,  $\mu'_s = 1.41 \text{ mm}^{-1}$  at both 650 nm and at 720 nm. For this experiment, after the measurement vector  $\mathbf{y}$  is simulated, we added Poisson noises with signal-to-noise ratios (SNR) of 20 dB ( $\approx 10\%$  noise), 10 dB ( $\approx 30\%$  noise) and 3 dB ( $\approx 57\%$  noise), where noise

(%) =  $100 \cdot \|\mathbf{A}\mathbf{f}^* - \mathbf{y}\|_2 / \|\mathbf{y}\|_2$ . Fig. 1 shows the true signal ( $\mathbf{f}^*$ ), the noise free measurements ( $\mathbf{A}\mathbf{f}^*$ ), and the observed photon count vector  $\mathbf{y}$  for the case SNR  $\approx 3$  dB.

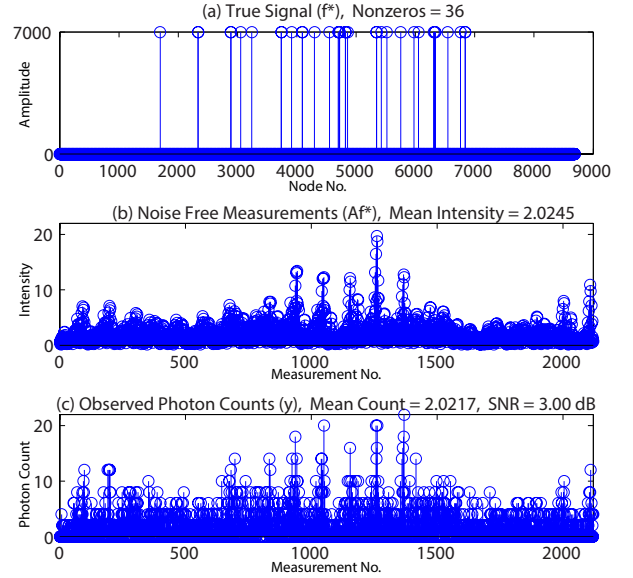


**Fig. 1.** Experimental setup. (a) True signal ( $\mathbf{f}^*$ ) of size 8,690 with 36 nonzero entries. (b) Noise free measurements ( $\mathbf{A}\mathbf{f}^*$ ) of size 2,120. (c) Very low mean photon count measurements ( $\mathbf{y}$ ) with 57% Poisson noise (SNR  $\approx 3$  dB). Note that the dimension of the measurement vector  $\mathbf{y}$  is four times smaller than the dimension of the true signal ( $\mathbf{f}^*$ ).

### 4. RESULTS

The reconstructed results for each method for different Poisson noise levels are shown in Table 1, and the corresponding detailed image quality metrics are given in Table 2. When the SNR is high (SNR  $\approx 20$  dB or 10% noise), we can see that all methods perform well. In general, NUMOS performs particularly well in obtaining more localized targets with high location accuracy. For low SNR measurements (SNR  $\approx 3$  dB), SPIRAL- $\ell_p$  method outperforms the NUMOS and SPIRAL- $\ell_1$  methods in obtaining locationally accurate targets with more strength. In the 30% Poisson noise experiment (SNR  $\approx 10$  dB), even though both the SPIRAL- $\ell_1$  and SPIRAL- $\ell_p$  methods perform quite well with relatively close image quality metrics, SPIRAL- $\ell_p$  image has very low background artifacts. For the SNR  $\approx 3$  dB setting, on average, SPIRAL- $\ell_p$  requires about 30 seconds for reconstruction, SPIRAL- $\ell_1$  requires 15 seconds, and NUMOS requires 3 seconds.

### 5. CONCLUSION

We proposed an approach for solving the FMT inverse problem when the observations are low-dimensional and are cor-

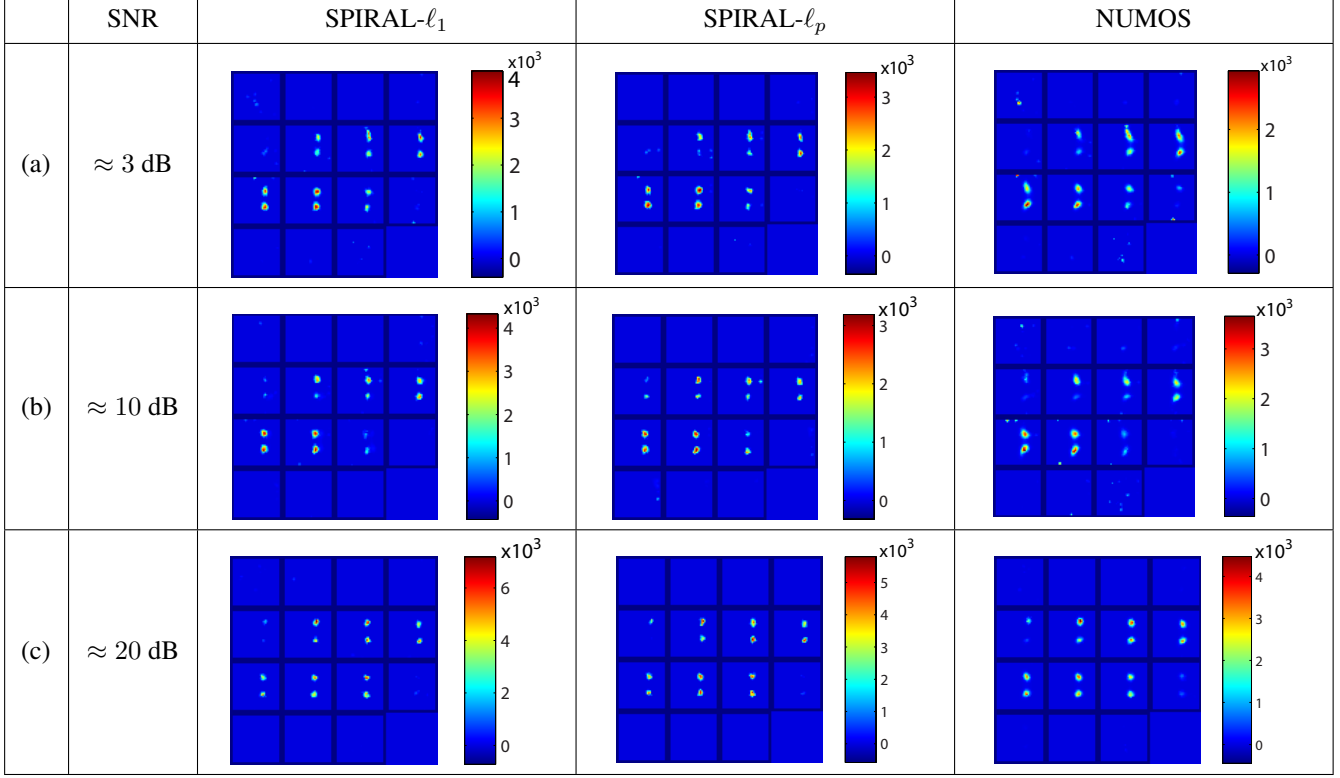


**Table 1.** Reconstructed horizontal slice images of the simulated cube using SPIRAL- $\ell_1$ , SPIRAL- $\ell_p$  ( $p = 0.74$ ) and NUMOS method: (a) when SNR  $\approx 3$  dB (57% Poisson noise), (b) when SNR  $\approx 10$  dB (30% Poisson noise), and (c) when SNR  $\approx 20$  dB (10% Poisson noise).

SNR	Algorithm	VR	Dice	CNR	MSE
$\approx 3$ dB	SPIRAL- $\ell_1$	0.95	0.30	7.40	$9.1 \times 10^4$
	<b>SPIRAL-<math>\ell_p</math></b>	<b>1.10</b>	<b>0.35</b>	<b>7.90</b>	<b><math>8.8 \times 10^4</math></b>
	NUMOS	1.10	0.32	7.20	$9.3 \times 10^4$
$\approx 10$ dB	SPIRAL- $\ell_1$	1.01	0.43	10	$7.0 \times 10^4$
	<b>SPIRAL-<math>\ell_p</math></b>	<b>0.98</b>	<b>0.47</b>	<b>10</b>	<b><math>7.8 \times 10^4</math></b>
	NUMOS	0.94	0.42	8.70	$8.3 \times 10^4$
$\approx 20$ dB	SPIRAL- $\ell_1$	0.73	0.61	16	$3.8 \times 10^4$
	SPIRAL- $\ell_p$	1.01	0.61	12	$5.5 \times 10^4$
	<b>NUMOS</b>	<b>0.94</b>	<b>0.63</b>	<b>14</b>	<b><math>4.5 \times 10^4</math></b>

**Table 2.** Metrics of the best reconstructions under different SNR levels ( $\approx 3$  dB, 10 dB, 20 dB) using SPIRAL- $\ell_1$ , SPIRAL- $\ell_p$  ( $p = 0.74$ ), and NUMOS algorithms. In the best case, VR and Dice metrics have to be close to 1 and the larger CNR is the better. Those best selections are in boldface letters.

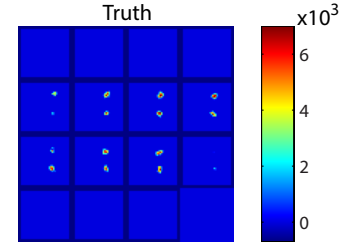


**Fig. 2.** The true image of the simulated cube.

rupted by Poisson noise. We assessed the performance of this approach on a simulated FMT cube and compared it to recently developed methods. According to the image quality metrics, we have shown that the nonconvex Poisson noise-based reconstruction method (SPIRAL- $\ell_p$ ) is particularly effective in low SNR settings. In near future, we will validate the effectiveness of the SPIRAL- $\ell_p$  method for low-dimensional actual phantom data in Poisson context.

## 6. REFERENCES

- [1] V. Ntziachristos, "Fluorescence molecular imaging," *Annual Review of Biomedical Engineering*, vol. 8, pp. 1–33, August 2006.
- [2] S. R. Cherry, "In vivo molecular and genomic imaging: new challenges for imaging physics," *Phys Med Biol*, vol. 49, pp. R13–48, Feb 2004.
- [3] J. K. Willmann, N. van Bruggen, L. M. Dinkelborg, and S. S. Gambhir, "Molecular imaging in drug development," *Nature Reviews Drug Discovery*, vol. 7, pp. 591–607, July 2008.
- [4] D. Han, J. Tian, S. Zhu, J. Feng, C. Qin, B. Zhang, and X. Yang, "A fast reconstruction algorithm for fluorescence molecular tomography with sparsity regularization," *Opt. Express*, vol. 18, no. 8, pp. 8630–8646, 2010.
- [5] C. Li, G. S. Mitchell, J. Dutta, S. Ahn, R. M. Leahy, and S. R. Cherry, "A three-dimensional multispectral fluorescence optical tomography imaging system for small animals based on a conical mirror design," *Opt. Express*, vol. 17, no. 9, pp. 7571–7585, Apr 2009.
- [6] X. Song, D. Wang, N. Chen, J. Bai, and H. Wang, "Reconstruction for free-space fluorescence tomography using a novel hybrid adaptive finite element algorithm," *Optics Express*, vol. 15, pp. 18300–18317, 2007.
- [7] D. Wang, X. Song, and J. Bai, "Adaptive-mesh-based algorithm for fluorescence molecular tomography using an analytical solution," *Opt. Express*, vol. 15, pp. 9722–9730, Jul 2007.
- [8] B. K. Natarajan, "Sparse approximate solutions to linear systems," *SIAM J. Comput.*, vol. 24, pp. 227–234, 1995.
- [9] R. Tibshirani, "Regression shrinkage and selection via the lasso," *Journal of the Royal Statistical Society, Series B*, vol. 58, pp. 267–288, 1994.
- [10] D. Zhu and C. Li, "Nonconvex regularizations in fluorescence molecular tomography for sparsity enhancement," *Physics in Medicine and Biology*, vol. 59, no. 12, pp. 2901–2912, 2014.
- [11] D. Zhu and C. Li, "Nonuniform update for sparse target recovery in fluorescence molecular tomography accelerated by ordered subsets," *Biomed. Opt. Express*, vol. 5, no. 12, pp. 4249–4259, Dec 2014.
- [12] J. Yu, J. Cheng, Y. Hou, and X. He, "Sparse reconstruction for fluorescence molecular tomography via a fast iterative algorithm," *Journal of Innovative Optical Health Sciences*, vol. 07, no. 03, pp. 1450008, 2014.
- [13] Z. T. Harmany, R. F. Marcia, and R. M. Willett, "This is SPIRAL-TAP: Sparse Poisson intensity reconstruction algorithms; theory and practice," *Image Processing, IEEE Trans. on*, vol. 21, no. 3, pp. 1084–1096, March 2012.
- [14] L. Adhikari and R. F. Marcia, "Nonconvex relaxation for poisson intensity reconstruction," Accepted to *2015 IEEE International Conference on Acoustics, Speech and Signal Processing*, 2015.
- [15] F. Fedele, J. P. Laible, and M. J. Eppstein, "Coupled complex adjoint sensitivities for frequency-domain fluorescence tomography: theory and vectorized implementation," *Journal of Computational Physics*, vol. 187, no. 2, pp. 597–619, 2003.
- [16] D. L. Snyder and M. I. Miller, *Random Point Processes in Time and Space*, Springer, 1991.
- [17] J. A. Fessler and A. O. Hero, "Penalized maximum-likelihood image reconstruction using space-alternating generalized em algorithms," *IEEE Trans. on Image Proc.*, vol. 4, no. 10, pp. 1417–1429, Oct 1995.
- [18] W. Zuo, D. Meng, L. Zhang, X. Feng, and D. Zhang, "A generalized iterated shrinkage algorithm for non-convex sparse coding," in *IEEE International Conference on Computer Vision (ICCV)*, Dec 2013, pp. 217–224.
- [19] F. Tian, G. Alexandrakis, and H. Liu, "Optimization of probe geometry for diffuse optical brain imaging based on measurement density and distribution," *Appl. Opt.*, vol. 48, no. 13, pp. 2496–2504, 2009.
- [20] L. R. Dice, "Measures of the amount of ecologic association between species," *Ecology*, vol. 26, pp. 297–302, 1945.
- [21] X. Song, B. W. Pogue, S. Jiang, M. M. Doyley, H. Dehghani, T. D. Tosteson, and K. D. Paulsen, "Automated region detection based on the contrast-to-noise ratio in near-infrared tomography," *Appl. Opt.*, vol. 43, pp. 1053–1062, 2004.